Polyaniline Doped with Dimethyl Sulfate as a Nucleophilic Dopant and Its Electrochemical Properties as an Electrode in a Lithium Secondary Battery and a Redox Supercapacitor

Kwang Sun Ryu,*,† Sang Kook Jeong,‡ Jinsoo Joo,§ and Kwang Man Kim*,†

Ionics Devices Team, Electronics and Telecommunications Research Institute, Daejon 305-700, South Korea, Nano Chem-Tech, Yongin 449-885, South Korea, and Department of Physics, Korea University, Seoul 136-701, South Korea

The physical properties of polyaniline (PAn) powder, doped by nucleophilic doping of dimethyl sulfate (DMS), were characterized, as well as its electrochemical behaviors, to investigate the possibility of a power source device adopting the PAn–DMS electrodes. It is shown that the nucleophilic addition of DMS into PAn concurrently resulted in an increase of the charge transport properties (e.g., electrical conductivity) and enhanced the processability (e.g., lowering of the melting point). The surface structure of PAn–DMS electrodes showed that the compactness of the electrode surface was helpful in increasing the capacity of lithium rechargeable batteries, whereas the porous behavior was valuable to improve the capacitance of a redox supercapacitor. Depending on the power source devices using the lump- and sheet-type PAn–DMS electrodes, the following optimized performances were obtained: more than 80 mA h g^{-1} after 50 cycles for lithium secondary battery use and ~115 F g^{-1} initially and ~94 F g^{-1} after 5000 cycles at a current density of 2.5 mA cm^{-2} for application as a redox supercapacitor, which were the highest reported performances for all PAn-based electrodes.

Introduction

Studies of synthesis, characterization, and application of conducting polymers such as polypyrrole, polythiophene, and polyaniline (PAn) have been widely performed over the past three decades because of the potential use of these polymers as key materials in various electrochemical devices. Of these, PAn has attracted great interest due to its high conductivity, stability in atmospheric environments, good processability, and ease of preparation. Early studies of PAn were concentrated on doping with various protonic acids.[1-6] In particular, the PAn salt form, doped with HCl, exhibited environmental stability and high conductivity at room temperature but poor processability in the doped state due to its insolubility in normal solvents, which induced high intermolecular interactions (hydrogen bonding) by chloric ions. Thereafter, many experiments have tried to improve the processability of PAn. Solubility increases were reported in the case of redox doping by FeCl$_3$.[7] Cao et al.[8] also reported that if a protonic acid with a bulky group, such as camphorsulfonic acid or dodecylbenzene sulfonic acid, was used as a dopant, then increases in the solubility in nonpolar solvents, the crystallinity of the PAn chain, and electrical conductivity up to 100–400 S cm^{-1} resulted. Thus, the studies of PAn afterward have been aimed at concurrently improving processability and electrical conductivity.

In general, doping of PAn can be divided into protonic doping and redox doping. Recent studies have primarily focused on protonic acid doping by the basicity of the imine site. The amino addition reaction by the electron donor of the imine site has been rarely discussed in these studies. In general, a strong nucleophile may act as a strong base, and therefore, the basicity and nucleophilicity may have the same meaning. Different bonding, however, can be formed by the base reaction (Figure 1a) if it interacts with a proton or by the nucleophile reaction (Figure 1b) with carbon. Wei et al.[9] reported that an amino addition reaction may occur between the nonbonding electrons in the N atom of emeraldine base PAn and the fullerene anion (C$_{60}$$^-$) as a good electron donor and acceptor, respectively. However, the PAn–C$_{60}$ system showed low conductivity of approximately 10^{-7} S cm^{-1} due to the weak interaction between the PAn and the fullerene anion caused by the steric hindrance of the large C$_{60}$ molecule.

The nucleophilic substitution reaction depends strongly on the substrate attacking nucleophiles. Molecules containing electron-affine carbon atoms with good leaving groups are very promising as substrates. Moreover, the carbon atoms should not be sterically hindered for the nucleophilic attack. In the present work, we used dimethyl sulfate (DMS) as a substrate satisfying the conditions mentioned above. The doping mechanism of DMS to PAn can be expected to follow the reaction scheme shown in Figure 1c. The synthesis and some characterizations of PAn doped with DMS are first performed in terms of the identification of chemical species, electrical conductivity, and dissolution effects for some protic solvents. The electrodes consisting of PAn–DMS were then prepared in both lump- and sheet-type forms, and their electrochemical properties were tested using them in both lithium secondary battery and redox supercapacitor devices. In the sheet-type PAn–DMS electrode, the effect of composition was investigated to determine the optimum formulations, resulting in best performances in the battery and capacitor applications.

* Authors to whom correspondence should be addressed. Phone: +82-42-860-5517 (K.S.R.); +82-42-860-6829 (K.M.K.). Fax: +82-42-860-6836 (K.S.R.); +82-42-860-6836 (K.M.K.). E-mail: ryuks@etri.re.kr (K.S.R.); kwang@etri.re.kr (K.M.K.).
† Electronics and Telecommunications Research Institute.
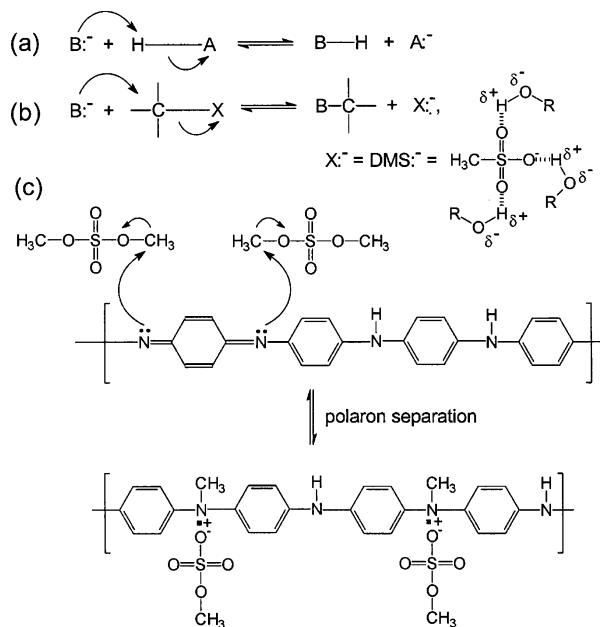‡ Nano Chem-Tech.
§ Korea University.

Figure 1. Reaction schemes of (a) doping by basicity (protonic acid doping), (b) doping by nucleophile, and (c) nucleophile doping of PAn with DMS.

Experimental Section

Synthesis of PAn−DMS. First, emeraldine base PAn (approximately 1 g) was synthesized by a chemical polymerization method previously reported.[10] To decrease as much as possible the crystallinity and the cross-link density of the emeraldine base PAn synthesized, doping with 1 M HCl aqueous solution and subsequent dedoping with a 1 M NH$_4$OH aqueous solution were repeated twice. This was then filtered by using a Buchner filter with 2 L of 0.1 N NaOH and finally with 2 L of acetone. The wet emeraldine base, after filtering, was mixed with 100 mL of a 1 M DMS aqueous solution at 40−60 °C for 16 h to yield a homogeneous dark green solution. Additional filtering and washing with acetone were repeated to remove the water component and the remaining unconsumed DMS until the filtered solution became transparent. Room-temperature drying of the precipitate resulted in the green powder of PAn−DMS.

Characterizations of PAn−DMS. Solvation properties were tested by dissolving the PAn−DMS powder into the various solvents of chloroform, formic acid, dimethylsulfoxide, dimethylformamide, ethylene glycol, *N*-methyl-2-pyrrolidone, *m*-cresol, and toluene. The amount of PAn−DMS powder was fixed as 3 wt % for each amount of solvent in this solvation test. For solvents in which PAn−DMS was soluble, the effect of solvation was examined by using UV−vis spectroscopy (Shimadzu UV-3501 spectrophotometer) in the wavelength range of 1000−250 nm. To identify the chemical species during doping of HCl and DMS, Fourier transform infrared spectroscopy (using a Magna-IR 560, Nicolet) was also performed in the wavenumber range of 4000−400 cm^{-1} for the pristine PAn, PAn−HCl, and PAn−DMS samples. Microscopic imaging of PAn−DMS powder was performed by using a field-emission scanning electron microscope (Philips SL30SFEG) at the magnification of 40 000×. Thermal behaviors and crystalline properties of PAn−HCl and PAn−DMS were also investigated by using a DSC/TGA SDT 2960 (TA Instruments) in the range of 25−300 °C at a heating rate of 10 °C min^{-1} and by using an X-ray diffractometer (Cu−Kα target, Rigaku) in the Bragg angle range of 10−45°, respectively. For the samples of PAn−HCl and PAn−DMS, direct current (dc) conductivity, σ_{dc}, was
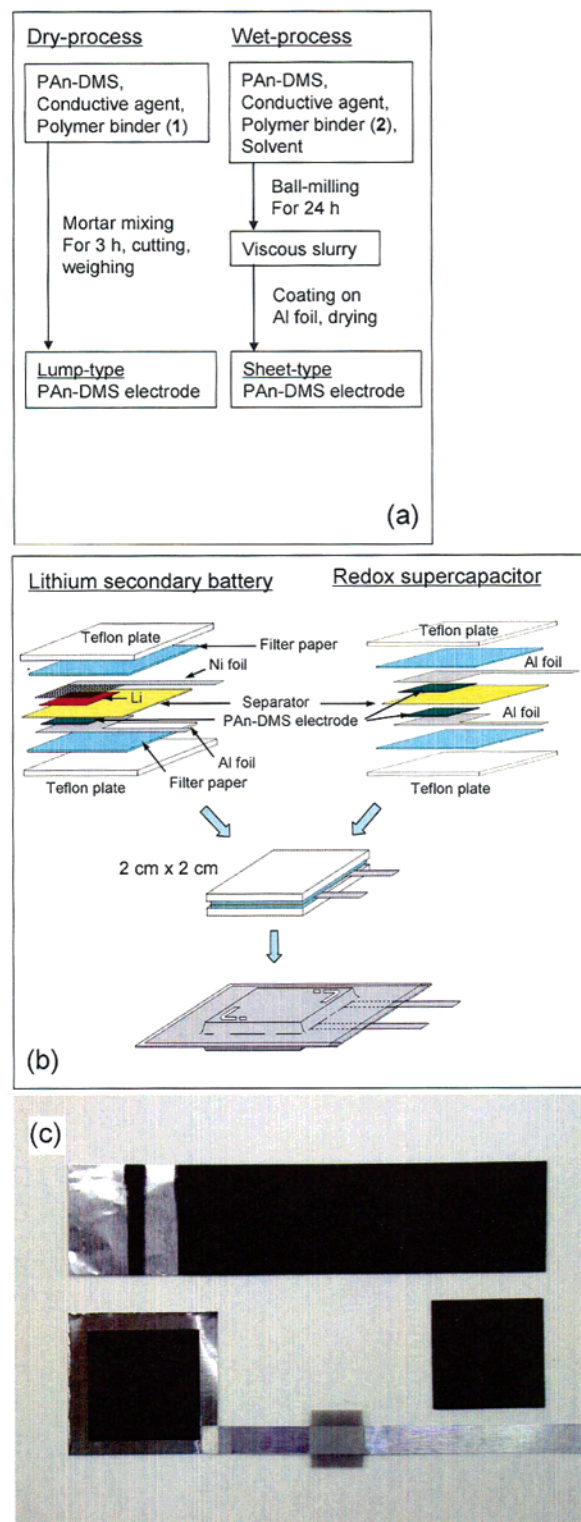

Figure 2. Schematic diagrams of (a) the preparation steps for PAn−DMS electrodes by dry and wet processes and (b) the fabrication procedure for sandwich cells in the form of a lithium secondary battery and a redox supercapacitor. (c) Image of a sheet-type PAn−DMS electrode that was coated on an aluminum foil, cut to give a 2 cm × 2 cm sized one, and finally placed on an aluminum tab.

measured at room temperature as a function of doping time and concentration of dopants by a standard four-probe Van der Pauw method. In addition, the temperature dependence of dc conductivity was also examined for the PAn−DMS sample in the range of 100−280 K.

Polyaniline Doped with Dimethyl Sulfate

J. Phys. Chem. B, Vol. 111, No. 4, 2007 **733**

TABLE 1: Compositions of PAn−DMS Electrodes and Their Applications in This Work

code	composition (wt %)				σ_{dc} at 25 °C (S cm^{-1})	application
	PAn−DMS	super P	PVB	PVdF-HFP		
VB-1	53.2	22.8	24.0		0.77	battery, capacitor
VB-2	58.7	25.2	16.1		0.93	battery, capacitor
VB-3	64.6	17.2	18.2		0.63	battery
VB-4	67.3	15.9	16.8		0.46	battery
VB-5	71.0	14.1	14.9		0.47	battery
VdF-1	56.1	24.1		19.8	0.58	battery, capacitor
VdF-2	43.8	18.7		37.5	1.25	capacitor
VdF-3[a]	43.8	18.7		37.5	1.36	capacitor

[a] In this case, the electrode was laminated on the expanded aluminum mesh as a current collector.

TABLE 2: Qualitative Summary of the Solvation Properties of PAn−DMS in Various Solvents and the Possibility of Obtaining a Self-Supporting Film

solvent	dielectric constant at 20 °C	degree of solvation	possibility of self-supporting film
chloroform	4.8	insoluble	no
m-cresol	9−11	soluble	yes
dimethylsulfoxide	55.0	very soluble	yes
dimethylformamide	36.7	soluble	no
ethylene glycol	37.0	soluble	yes
formic acid	58.0 (at 15.5 °C)	very soluble	yes
N-methyl-2-pyrrolidone	32.3	soluble	no
toluene	2.4	insoluble	no

Preparation of PAn−DMS Electrodes. Two types of PAn−DMS electrodes were prepared by dry and wet processes (Figure 2a). In the dry process, raw materials of PAn−DMS powder, carbon black (Super P, MMM Carbon) powder as a conductive agent, and poly(tetrafluoroethylene) powder (Aldrich) as a polymer binder were mixed together in a mortar for 3 h with the weight ratio of 8:2:1, respectively. The mixture was then spread on aluminum foil (15 μm thick) to give the lump-type PAn−DMS electrode. In the wet process, a proper amount of acetone solvent was additionally used to make viscous slurry via moderately severe ball-milling for 24 h. It should be noted that the polymer binder in the wet process can be different from the case of the dry process because a polymer binder with good solubility in the solvent must be used to produce a homogeneous slurry in a highly dispersed state. In this wet process, poly-(vinylidene fluoride-*co*-hexafluoropropylene) (PVdF-HFP; KynarFlex 2801, Atofina Chemicals) and poly(vinyl butyral) (PVB; Aldrich) were used as polymer binder materials with their precise compositions listed in Table 1. The viscous slurry was then coated on aluminum foil by using a doctor blade apparatus, and the solvent component was evaporated under an ambient atmosphere to give the sheet-type PAn−DMS electrode (refer to the image in Figure 2c). However, sample VdF-3 in Table 1 was prepared by laminating the PAn−DMS electrode on the expanded aluminum mesh as a current collector without using the aluminum foil. For some sheet-type PAn−DMS electrodes, surface morphologies were observed by using a field-emission scanning electron microscope (Philips SL30SFEG) at a magnification of 80 000×.

Fabrications of Battery and Capacitor. As applications of the PAn−DMS electrodes in the present work, prototype lithium secondary battery and redox supercapacitor cells were fabricated following the schematic diagram in Figure 2b. In both sides of the battery and capacitor, glass filter paper, as a reservoir of electrolyte solution, and a Teflon plate, as a solid supporter, were placed on the surface before sealing with a plastic pouch. The main scheme of the lithium secondary battery was a sandwich form, which consisted of lithium foil attached to a thin nickel plate as an anodic current collector, a sheet of porous polyethylene separator (Celgard), and a PAn−DMS electrode

(lump- or sheet-type, 2 cm × 2 cm) on thin aluminum foil as a cathodic current collector. The redox supercapacitor had a similar sandwich form, but its constituents were somewhat different in that it consisted of two PAn−DMS electrodes (lump- or sheet-type, 2 cm × 2 cm) on thin aluminum foils, which were divided by a sheet of a porous polyethylene separator. The electrolyte solution, enough to sufficiently wet the electrode element, was injected just before vacuum-sealing with a plastic pouch. The electrolyte solution was 1 M of LiPF$_6$, dissolved in a mixture of ethylene carbonate and dimethyl carbonate (1:1 (v/v)), for the lithium secondary battery and 1 M of tetraethylammonium tetrafluoroborate (Et$_4$NBF$_4$), dissolved in propylene carbonate, for the redox supercapacitor. The electrolyte injection and vacuum-sealing occurred in a dry room in which the moisture content was kept below 0.1 ppm.

Performance Measurements of the Battery and Capacitor. The lithium secondary battery and redox supercapacitor were characterized by using electrochemical measurements. Electrical impedance spectra were obtained with a frequency response analyzer (Solartron SI 1260), connected with a potentiostat (Solartron 1287), in a frequency range from 0.1 Hz to 1 MHz. Cyclic voltammetry was also performed, using a MacPile II potentiostat system at a scan rate of 10 mV s^{-1}. The potential ranges were 1.5−4.5 V vs Li/Li$^+$ for the lithium secondary battery and 0.0−1.0 V vs Ag/AgCl for the redox supercapacitor. The lithium secondary battery was tested by using a galvanostatic charge−discharge cycler (Toscat-3000, Toyo Systems) in the range of 2.0−4.0 V, with a constant current density of 0.025 mA cm^{-2}. The redox supercapacitor was also tested by using the same cycler in the range of 0.0−1.0 V under the charging condition of constant current density and the subsequent constant voltage of 1.0 V for 5 min. Discharge was performed with the same constant current density. In the redox supercapacitor, the constant current density applied was 1.25 mA cm^{-2} for the lump-type electrode and was varied from 0.5 to 2.5 mA cm^{-2} for the sheet-type electrode.

Results and Discussion

Solvation of PAn−DMS. PAn is very insoluble in polar solvents because of the nonpolarity of the aromatic compound.
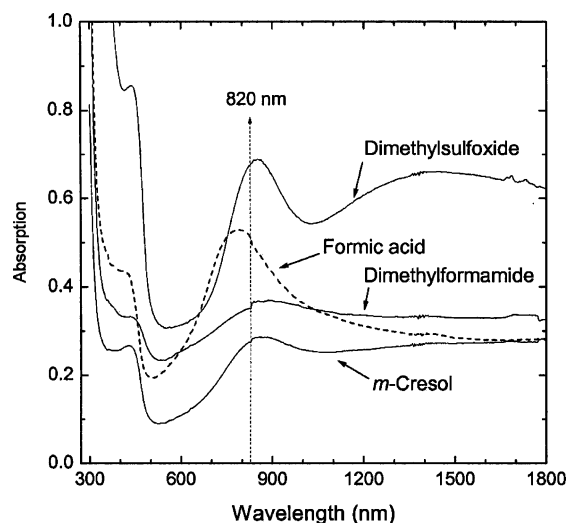
Figure 3. UV spectra of PAn−DMS in various solvents to examine its solvation effects. The amount of PAn−DMS powder was fixed at 3 wt % for each amount of solvent in this solvation test.

Figure 4. Fourier transform infrared spectra of PAn, PAn−HCl, and PAn−DMS.

However, the PAn−DMS is soluble in the polar solvents with a high dielectric constant, such as dimethylsulfoxide, formic acid, ethylene glycol, and *m*-cresol (Table 2). In general, the solubility increased due to the affinity of the similar chemical structures between polymer and solvent molecules, as in the expression "like dissolves like". The solvation of the polymer results from the dissolution and penetration of solvent into polymer chains, which manifests stronger interactions between polymer and solvent than existed between polymer and polymer. DMS used as the dopant in this work has a bulky dimension that lengthens the distance between the polymer chains. Moreover, the affinity between the polymer chain and the solvent can be enhanced to enable solubility in a polar solvent if a polar solvent with substitutable groups similar to the sulfate of DMS, such as dimethylsulfoxide, is used. Table 2 summarizes the solvation properties of PAn−DMS in various solvents and the possibility of obtaining its self-supporting film. PAn−DMS was insoluble in water but can produce its free-standing film in ethylene glycol in which it was totally insoluble when doping with protonic acid.

Figure 3 shows the ultraviolet spectroscopy results upon examination of the solvation effect of various soluble solvents for PAn−DMS. Most of the solvents display localized polaron peaks at 820 nm, corresponding to the localization of charge carriers by π-polaron transition.[11] This is regarded to be due to the increase in the torsion (dihedral) angle between phenyl rings by the doping of the methyl group, which is larger than the hydrogen atom. The $\pi-\pi^*$ electron transition within benzenoid segments at 360 nm is absent, and the polaron band at 435 nm is observed relating to the doping level or formation of polarons.[12] However, broad, near-infrared absorption peaks at 1000−1500 nm appear due to the delocalization of charge carriers when using dimethylsulfoxide and *m*-cresol. These are demonstrated as good solvents for PAn−DMS due to the hydrogen bonding and the solvation effect between the counteranion (DMS− in Figure 1) and the polymer chain. In addition, PAn−DMS dissolved in formic acid exhibits slightly shifted peaks at 420 and 800 nm to a lower wavelength region in comparison to the peaks at 435 and 820 nm of other solvents. It is probably due to the high acidity of the solvent, which may cause the exchange of DMS− and H+ to yield a higher solubility.

Characteristics of the PAn−DMS Powder. Infrared spectroscopy was performed for the PAn salt powder doped with
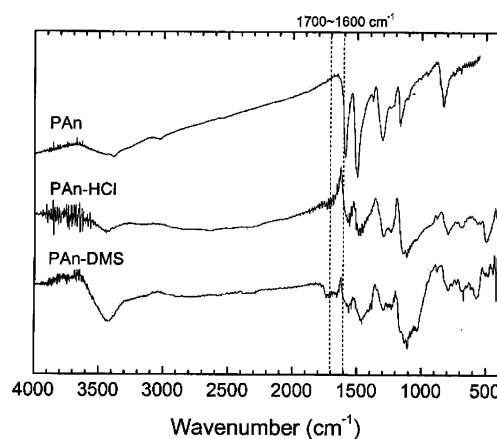
DMS at 60 °C to confirm the formation of the N−CH$_3$ bond by doping the methyl group of DMS to the imine site of PAn during the nucleophilic addition reaction of emeraldine base PAn. As shown in Figure 4, the as-prepared PAn and the PAn doped with protonic acid (HCl) were also examined for comparison. The infrared assignments of PAn, PAn−HCl, and PAn−DMS are listed and compared with the previous results[13−15] in Table 3. This result is reliable because the resonance stabilization by the presence of the counteranion (DMS−) leads to the peak shifts to lower wavenumbers.[15] Actually, the doping of DMS was rapidly accomplished just after the solvation, whereas very slow doping occurs when using lithium ionic salts.[13] In addition, it is very noteworthy that new peaks appeared at the band of 1600−1700 cm^{-1} for PAn−DMS that did not appear in the case of PAn−HCl. These peaks may correspond to a N−CH$_3$ bond formed by a nucleophilic amino addition reaction.

Figure 5a shows the PAn−DMS powder morphology, which has many granular aggregates with an average particle size of 100−200 nm. In contrast to the case of using camphorsulfonic acid[16] as a dopant, a less porous structure was developed. The aggregates, however, showed a less compact morphology than the case of using poly(styrene sulfonic acid)[16] as a dopant. This can be considered as an intermediate property of DMS between camphorsulfonic acid and poly(styrene sulfonic acid) in terms of surface compactness. Though the DMS is less bulky than these protonic dopants, it seems that the nucleophilic addition of DMS can provide sufficient morphology to simultaneously improve the electrochemical properties (e.g., electrical conductivity) and the processability, which are comparable to cases in which protonic dopants are used.

Melting at moderate temperatures is required for the processability of PAn−DMS. Though some weight loss of approximately 30 wt % occurred, processable PAn−DMS melting is possible around 250 °C, whereas the pristine PAn did not show any melting or weight loss even at 300 °C, as shown in Figure 6a. In general, pristine PAn starts to decompose around 500 °C, but the PAn's doped with various sulfonic acids can decompose below 250 °C.[16,17] The first broad endothermic peak and corresponding weight loss of approximately 15 wt % in the range of 40−110 °C reflects the evaporation of residual water remaining after the filtering and drying in the preparation of the PAn−DMS powder. The humid component can be removed if further drying is applied. The second endothermic peak and weight loss of approximately 30 wt % at 250 °C may be considered to be due to the breakage of hydrogen bonding and/or the cleavage and removal of DMS anions from the PAn

TABLE 3: Assignments and Comparison of Infrared Spectra for PAn, PAn−HCl, and PAn−DMS

	wavenumber (cm^{-1})						
sample	NQN[a]	NBN[b]	C−N[c]	C−N[d]	QNH$^+$B[e]	C−H[f]	aromatic[g]
PAn	1590	1497	1379, 1301	1214	1165	829	
PAn[h]	1593	1503	1379, 1306	1238	1166	833	
PAn−HCl	1557	1487	−, 1290	1244	1111	791	486
PAn−HCl[i]	1559	1483	−, 1298		1108	795	561
PAn−HCl[j]	1579	1493	−, 1292		1143	822	
PAn−DMS	1560	1459	−, 1286	1230	1106	786	569

[a] Stretching of the quinoid (Q) diimine unit. [b] Stretching of the benzenoid (B) diimine unit. [c] C−N stretchings in the QBQ, QBB, and BBQ series. [d] C−N stretching in the BBB series. [e] A mode of QNH$^+$B. [f] C−H out-of-plane bending. [g] Aromatic ring deformation [h] Reference 13. [i] Reference 14. [j] Reference 15.
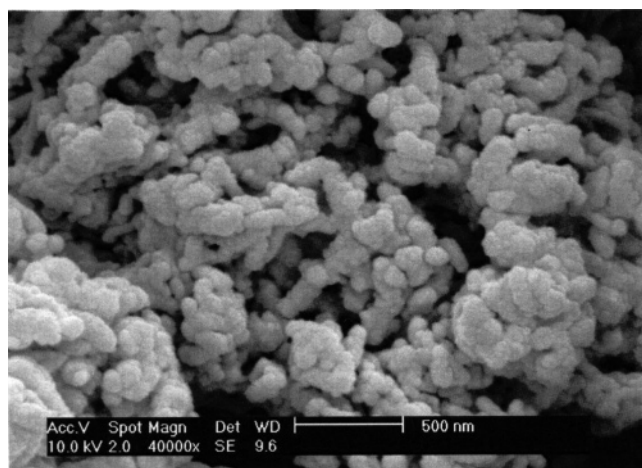

Figure 5. Field-emission scanning electron microscopic images of PAn−DMS with a magnification of 40 000×.
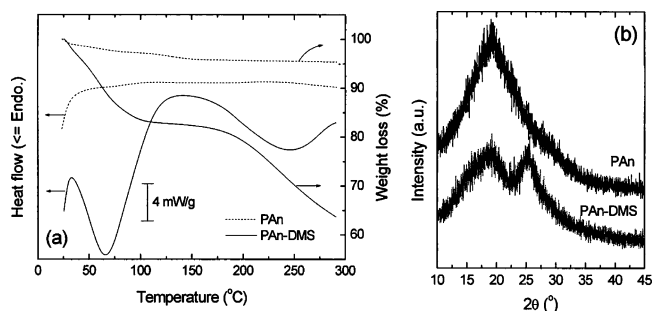

Figure 6. Results of (a) thermogravimetric analysis and differential scanning calorimetry and (b) X-ray diffraction analysis in the Bragg angle range of 10−45°.

Figure 7. Electrical conductivities of PAn−HCl and PAn−DMS measured at 60 °C as functions of (a) doping time and (b) dopant concentration. The pH in the upper *x*-axis of part b corresponds negatively to the concentration of HCl.

chains. The X-ray diffraction patterns of PAn and PAn−DMS clearly exhibit amorphous and partially crystalline features in Figure 6b. It seems that the fusion of the crystal phase of PAn−DMS corresponds to the broad melting peak around 250 °C and that it enables processability at moderate temperatures around 200−250 °C without a decrease in electrochemical properties (e.g., electrical conductivity). In addition, the peak at $2\theta \approx 20°$ corresponds to the close-contact interchain distance.[18] Also, the peaks at $2\theta \approx 20°$ and ∼25° represent the periodicities parallel (100) and perpendicular (110) to the PAn chains, respectively.[19] Thus, it can be deduced from Figure 6b that PAn−DMS can possess high crystallinity, in comparison to bare Pan, due to the stereoregularity of PAn chains with the help of DMS salt.

Electrical Conductivity. The doping reaction of PAn by nucleophile addition using DMS easily occurred under the polar solvent, which plays the role of a stabilizing anion as a dissociated species. The polar solvent dissolves the DMS anion by the interaction between the ionic charge and the dipole
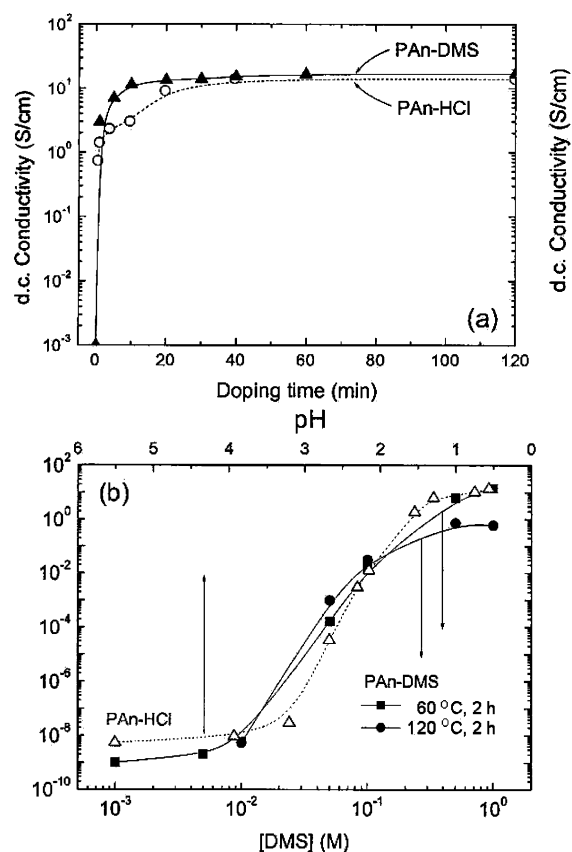
moment of the solvent. In particular, the dissociated anions create hydrogen bonding with the hydrogen atom of the −OH group (Figure 1b) in the protic solvents, such as water and alcohol. The stabilized dissociated group makes the reaction rate very fast and can result in a higher electrical conductivity than that in the case using a nonpolar solvent.

Comparable to doping with a protonic acid, the nucleophilic addition doping strongly depends on doping time, dopant concentration, and temperature. Figure 7 shows the electric conductivities for nucleophile-doped PAn−DMS and proton-doped PAn−HCl as functions of doping time and dopant concentrations. A more rapid increase in the conductivity occurred in PAn−DMS than in PAn−HCl, but their saturated values were nearly identical after about 40 min at ∼10 S cm^{-1}. The dependence of the conductivity also exhibited a similar trend to that of the increase in the dopant concentration. It is very important to note that the conductivity can be increased from 10^{-9} up to ∼10 S cm^{-1} by adjusting the concentration of the nucleophile dopant. That is, the transition from the insulating
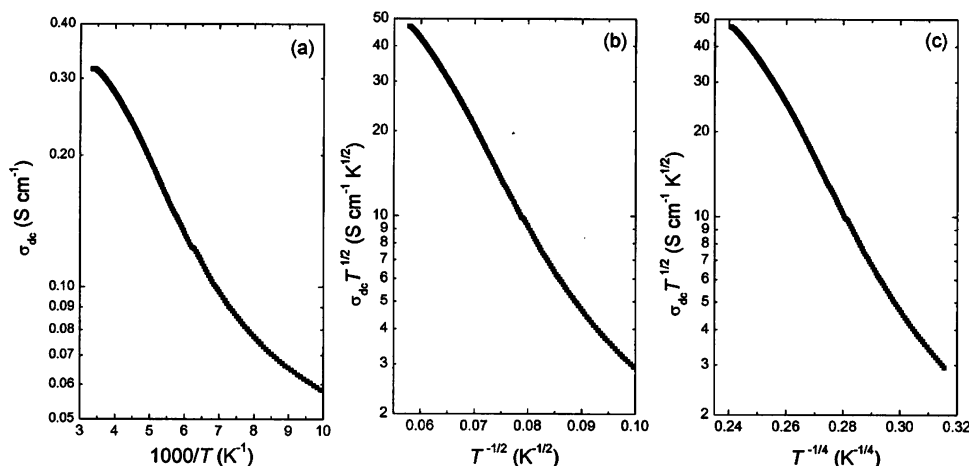
Figure 8. Electrical conductivity σ_{dc} of PAn−DMS as function of temperature T, which is expressed in relation to (a) an Arrhenius plot (ln σ_{dc} vs $1000/T$), (b) a one-dimensional Mott plot [ln($\sigma_{dc}T^{1/2}$) vs $T^{-1/2}$], and (c) a three-dimensional Mott plot [ln($\sigma_{dc}T^{1/2}$) vs $T^{-1/4}$].
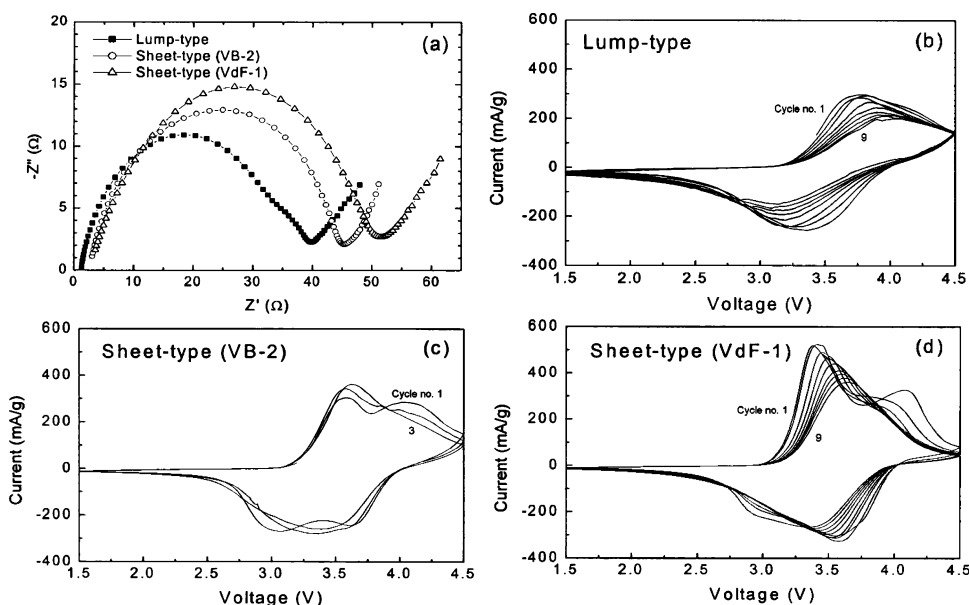

Figure 9. (a) Impedance spectra of battery cells including the PAn−DMS electrode, and cyclic voltammograms of battery cells of including (b) the lump-type PAn−DMS electrode and the sheet-type PAn−DMS electrode using the polymer binders of (c) VB-2 and (d) VdF-1. The voltage ranges in the cyclic voltammograms are based on the lithium electrode potential (Li/Li^{+}) for use in the lithium secondary battery.

state to the conducting state of the PAn system easily occurs by DMS doping via the onset of a transition at approximately 0.01 M of DMS.

The temperature dependence of electrical conductivity in conducting polymer has not yet been comprehensively understood though many models have been proposed for conduction in doped conducting polymers. Some models are known to be useful to adopt within a limited temperature range. One case is the Arrhenius equation

$$\sigma_{dc} = \sigma_0 \exp\left(-\frac{E_a}{kT}\right) \qquad (1)$$

where σ_{dc} denotes the electrical conductivity, σ_0 is the pre-exponential factor, E_a is the activation energy, k is the Boltzmann constant, and T represents the absolute temperature. Another example is the Mott-type variable range hopping model,[20] in which the conduction is treated as the hopping by thermal activation from center to center

$$\sigma_{dc} = A_0 T^{-1/2} \exp\left(-\left(\frac{T_0}{T}\right)^{1/(n+1)}\right) \qquad (2)$$

where

$$T_0 = 16\alpha^3/kN(E_F) \qquad (3)$$

$$A_0 = 0.39\nu_0 e^2 (N(E_F)/\alpha k)^{1/2} \qquad (4)$$

α is the inverse of decay length of the localized state, ν_0 is a hopping frequency, $N(E_F)$ is the state density of Fermi level, e is the electronic charge, T_0 is the Mott characteristic temperature, and A_0 is the Mott characteristic conductivity parameter. Here, n represents the dimensionality of conduction.

The Arrhenius and Mott (one- and three-dimensional) conductivity plots for PAn−DMS are shown in Figure 8. The activation energy, E_a, obtained from the slope of the Arrhenius plot in the temperature range of 140−208 K (linear range) was calculated as ∼0.013 eV. The conductivity data obtained for PAn−DMS did not yield a good linear plot for the Arrhenius equation, but Mott expressions gave good linear fits. While a quasi-one-dimensional Mott plot of ln σ_{dc} vs $T^{-1/2}$ easily lead to the best fit for the PAn−Li salt system,[21] Mott plots of ln($\sigma_{dc}T^{1/2}$) vs $T^{-1/(n+1)}$ were quite adequate to linearly fit the present PAn−DMS system, as shown in Figures 8b ($n = 1$)
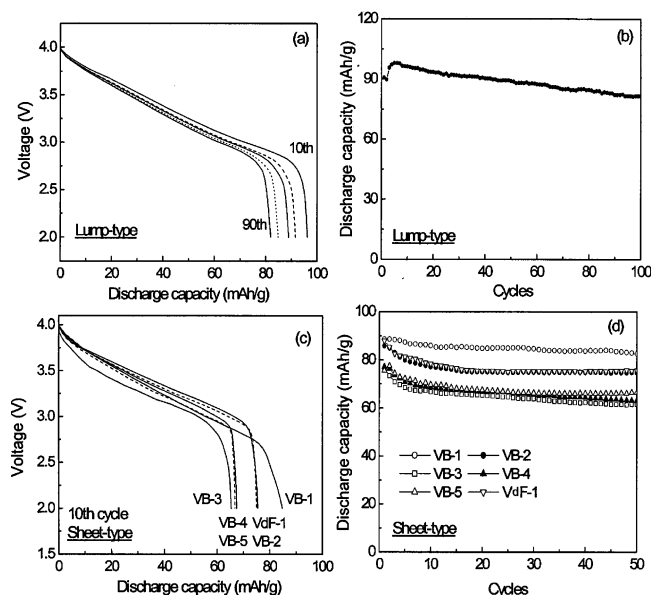
Figure 10. Capacity and cycle performances of the lithium secondary battery including the PAn−DMS electrode: (a) discharge capacity and (b) cyclability of the battery adopting the lump-type PAn-DMS electrode and (c) discharge capacity at the 10th cycle and (d) cyclability of the battery adopting the sheet-type PAn−DMS electrode using various polymer binders.

and 8c ($n = 3$). Both plots show nearly the same temperature range (135−260 K for $n = 1$ and 128−248 K for $n = 3$) corresponding to the linear fitting, but the Mott characteristic temperatures, T_0, calculated from the slope of linear fitting, are different and equal to 394 ($n = 1$) and 3.2×10^6 K ($n = 3$). In comparison with other cases[21] of PAn−Li salts whose T_0 values in a quasi-one-dimensional Mott model are higher than 1000

K, it can be determined that PAn−DMS is the most highly conducting sample. In addition, the lower activation energy of conduction, which was evaluated by an Arrhenius plot described above, is also evidence of the highly conducting behavior of the present PAn−DMS.

Lithium Secondary Battery. The electrochemical behaviors of the PAn−DMS electrode for lithium secondary battery use were examined in terms of complex impedance spectra and cyclic voltammograms, as shown in Figure 9. Capacity and cycle performances of the lithium secondary battery are also presented in Figure 10. A portion of these features was previously published,[22] but the results presented here are a fully upgraded version of the battery characteristics, including the effects of polymer binder materials. The internal resistances of batteries containing PAn−DMS electrodes were roughly estimated as 40 Ω for lump-type and 45−50 Ω for sheet-type electrodes (Figure 9a). It is known that the amount of polymer binder as an insulator in the electrode plays the role of determining the absolute value of the resistance. The content of polymer binder was 9 wt % for the lump-type electrodes and 16 and 20 wt % for the sheet-type electrodes (VB-2 and VdF-1, respectively). Moreover, the difference in the binding strength between PVB and PVdF-HFP binders may affect the resistance. As the polymer binder in the sheet-type electrode, the low content of PVB can replace the higher content of PVdF-HFP due to its higher binding strength and the capability for a more compact morphology of the electrode (Figure 11 and refer to the detailed description below).

Figures 9b−d are the results of cyclic voltammetry for the battery cells containing lump- and sheet-type electrodes in the range of 1.5−4.5 V (vs Li/Li$^+$) to investigate oxidation and reduction potentials and electrochemical reactions. The upper broad peaks at 3.5−3.8 V correspond to the oxidation and
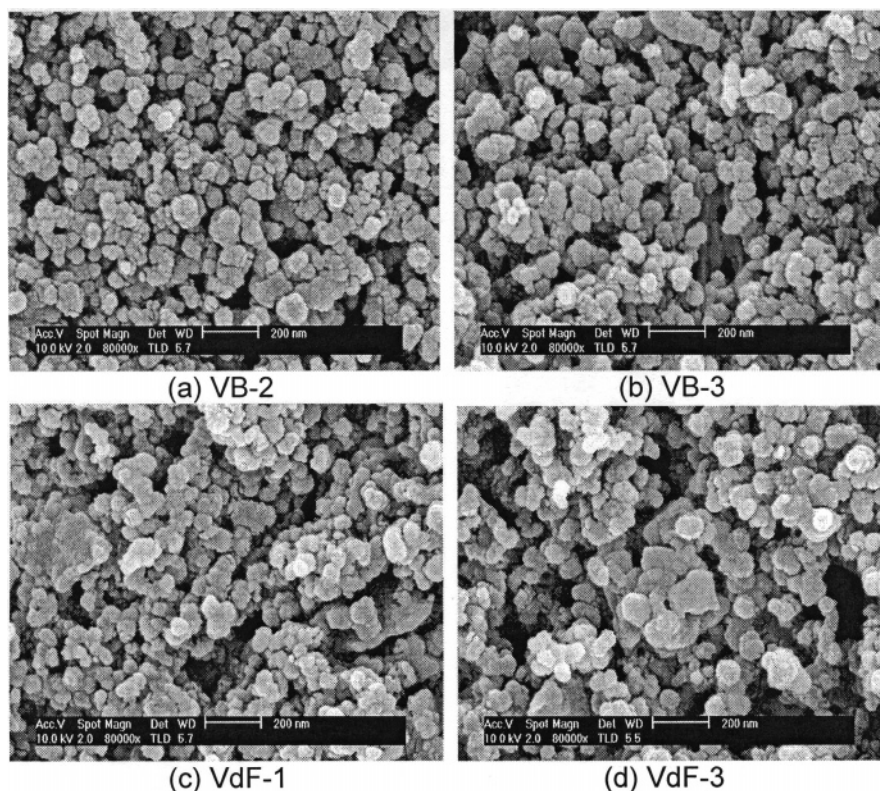

(a) VB-2   (b) VB-3   (c) VdF-1   (d) VdF-3

Figure 11. Field-emission scanning electron microscopic images of sheet-type PAn−DMS electrodes using different polymer binders of (a) VB-2, (b) VB-3, (c) VdF-1, and (d) VdF-3. In the case of VdF-3, the aluminum mesh (expanded metal) was used as a current collector instead of aluminum foil. The PAn−DMS electrodes of parts a−c were used to fabricate the battery cell, whereas those of parts a, c, and d were used for the capacitor cell.
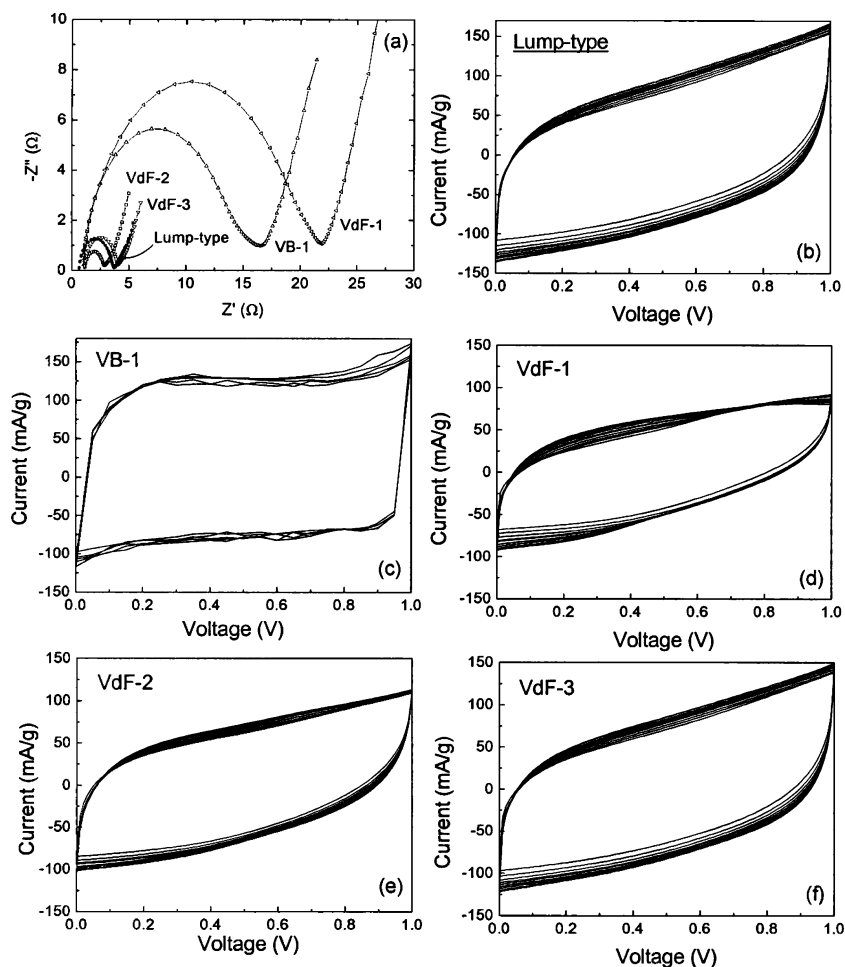
Figure 12. (a) Impedance spectra of capacitor cells containing the PAn−DMS electrode and cyclic voltammograms of battery cells containing (b) the lump-type PAn−DMS electrode and sheet-type PAn−DMS electrodes using the polymer binders of (c) VB-1, (d) VdF-1, (e) VdF-2, and (f) VdF-3. The voltage ranges in the cyclic voltammograms are based on the Ag/AgCl electrode for use in the redox supercapacitor.

p-doping reaction with CH_3^+ or $CH_3OSO_2O^-$, while the lower broad peaks at 3.2−3.5 V correspond to the reduction and undoping.[22] The intensity change of the lower peaks (reduction process) with repeated scans may result from the gradual fade of discharge capacity by the irreversible reaction of PAn−DMS within the battery system. It can be expected from a comparison of the cyclic voltammograms that the capacity fade is more strictly observed for the battery cell containing lump-type rather than sheet-type electrodes. This trend is present in the present study and is observable in Figure 10, which shows the enhanced cyclability of the sheet-type electrode compared to that of the lump-type electrode. In addition, it is very noteworthy that the specific discharge capacity of the lithium secondary battery using the PAn−DMS electrode was highly improved to more than 80 mA h g^{-1} after 50 cycles compared to ∼40 mA h g^{-1} for PAn−LiBF$_4$ and ∼50 mA h g^{-1} for PAn−LiPF$_6$ systems.[23,24] This value is probably the highest specific discharge capacity that has ever been reported in lithium secondary batteries using PAn-based electrodes.

Figure 10d shows the good cyclability of sheet-type PAn− DMS electrodes. The difference in the discharge capacity is probably due to the electrode morphology and the kind and content of polymer binder, compositions of active material and conductive agent, and finally the adhesion state between the particles. As shown in Figure 11, somewhat similar although different morphologies were observed for samples including different binders and contents. The images of Figure 11 show that PAn−DMS (main particle) was connected uniformly to the
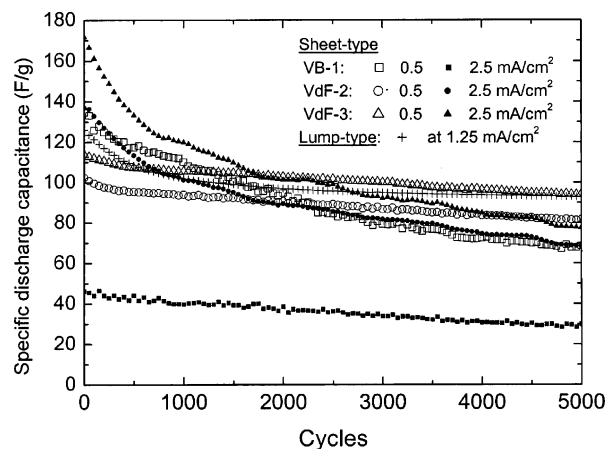

Figure 13. Cyclability results of the redox supercapacitor adopting lump- and sheet-type PAn−DMS electrodes at different current densities.

conductor (very small granules surrounding the particle) by means of a binder that was admixed with the particles to yield micropores on the surface of the electrode plate. In comparison with the case of the PAn−LiPF$_6$ electrode,[25] a more compact structure was observed in PAn−DMS electrodes with slightly different porosities. In Figure 11, the electrodes of VB-2 and VdF-1 had lower porosities with higher packing densities, which are favorable in efficient electrical transport to give high discharge capacities. Though a quantitative analysis would be required, the porosity or compactness of the electrode morphol-

Polyaniline Doped with Dimethyl Sulfate

J. Phys. Chem. B, Vol. 111, No. 4, 2007 **739**

ogy may be essentially associated with the capacity in the lithium secondary battery (and, moreover, with the capacitance in the redox supercapacitor). That is, the decrease in the porosity or the compactness of electrode structure lowers the capacity of the lithium secondary battery containing the PAn–DMS electrode.

Redox Supercapacitor. The redox supercapacitor cell containing the PAn–DMS electrode shows lower bulk resistance of the electrode/electrolyte solution than the lithium secondary battery, as shown in Figure 12a. The lower resistance is mainly due to the close contact of symmetric PAn–DMS electrodes divided by a sheet of porous polyethylene separator. In the redox supercapacitor, the surface (or contact) area between the electrode and the electrolyte is more important because a charge transfer occurs at the interface where the electric double layer is formed along the surface. The kind and the amount of polymer binder in the electrode do not greatly influence the capacitance, but the surface area does. That is, higher porosity increases the electrode contact area for the redox supercapacitor and, thus, increases its capacitance, which is opposite to the trend in the lithium secondary battery discussed above.

Cyclic voltammograms for the capacitor cells in Figures 12b–f have almost symmetrical and rectangular shapes, which are very similar to that of a typical voltammogram of an electrochemical capacitors. They also show very good reversibility during oxidation (doping) and reduction (dedoping) repeated over many cycles. This fact reflects the cyclability of capacitance. Except for the case of VB-1, the size of the voltammogram also decreased with an increase in the bulk resistance in Figure 12a, and it may correspond to the capacitance of the redox supercapacitor. Moreover, in association with the surface morphologies of the sheet-type electrodes in Figure 11, the higher surface area or porosity is related to the size increase of the cyclic voltammogram and consequently to the increase in discharge capacitance.

Figure 13 shows the specific discharge capacitances of redox supercapacitors using PAn–DMS electrodes. Though there appears to be a somewhat steep fade of capacitance in the initial stage, the capacitance stabilized with repeated charge/discharge cycles. High-rate (2.5 mA cm^{-2}) charge/discharge cycling resulted in a more severe capacity fade. Comprehensively analyzing both the capacitance and the cyclability, using the VdF-3 electrode was optimal and showed a higher capacitance of ~115 F g^{-1} initially and ~94 F g^{-1} at 5000 cycles at a current density of 2.5 mA cm^{-2}. In comparison to previous reports[25,26] using PAn–LiPF$_6$ electrodes that resulted in ~107 F g^{-1} initially and ~84 F g^{-1} at 9000 cycles at 1.25 mA cm^{-2}, these values presented here are the highest capacitances that have ever been achieved in redox supercapacitors using PAn-based electrodes. In particular, the enhanced performance of the redox supercapacitor using the VdF-3 electrode may be due to the close contact caused by laminating the PAn–DMS electrode sheet and current collector (aluminum mesh).

Concluding Remarks

We studied the physical characteristics of PAn powder doped by the nucleophilic addition of DMS, the electrochemical properties of Pan–DMS, and, finally, the performances of lithium secondary batteries and redox supercapacitors adopting PAn–DMS electrodes in lump- and sheet-type arrangements. The nucleophilic addition of DMS into PAn has the advantageous features of increasing the electrical conductivity and, simultaneously, enhancing the processability of the polymer melt. Also, the surface morphologies of the PAn–DMS electrodes provided insight about the performance of the electrochemical devices. The compactness of the surface structure was beneficial in increasing the capacity of the lithium rechargeable battery, whereas the porosity was useful for improving the capacitance of the redox supercapacitor. Therefore, the best performance results can be obtained for battery and capacitor use by adjusting the electrode morphology, which is associated with an adequate selection of the contents and constituents of the electrode.

References and Notes

(1) MacDiarmid, A. G.; Chiang, J. C.; Halpern, M.; Huang, W.; Mu, S.; Somasiri, N. L. D.; Wu, W.; Yaniger, S. T. *Mol. Cryst. Liq. Cryst.* **1985**, *121*, 173.

(2) Salaneck, W. R.; Lundstrom, I.; Hjertberg, T.; Duke, C. B.; Conwell, E.; Paton, A.; MacDiarmid, A. G.; Somasiri, N. L. D.; Huang, W. S.; Richter, A. F. *Synth. Met.* **1987**, *18*, 291.

(3) Vachon, D.; Angus, R. O., Jr.; Lu, F. L.; Nowak, M.; Lin, Z. X.; Schaffer, H.; Wudl, F. Heeger, A. J. *Synth. Met.* **1987**, *18*, 299.

(4) Wang, B.; Tang, J.; Wang, F. *Synth. Met.* **1987**, *18*, 323.

(5) Okabayashi, K.; Goto, F.; Abe, K.; Yoshida, T. *Synth. Met.* **1987**, *18*, 365.

(6) Rouleau, J. F.; Goyett, J.; Bose, T. K.; Singh, R.; Tandon, R. P. *Phys. Rev. B* **1995**, *52*, 4801.

(7) Han, C. C.; Elsenbaumer, R. L. *Synth. Met.* **1989**, *30*, 123.

(8) Cao, Y; Smith, P.; Heeger, A. J. *Synth. Met.* **1992**, *48*, 91.

(9) Wei, Y.; Tian, J.; MacDiarmid, A. G.; Masters, J. G.; Smith, A. L.; Li, D. *J. Chem. Soc., Chem. Commun.* **1993**, 603.

(10) Ryu, K. S.; Chang, S. H.; Kang, S.-G.; Oh, E. J.; Yo, C. H. *Bull. Korean Chem. Soc.* **1999**, *20*, 333.

(11) (a) Cao, Y; Smith, P.; Heeger, A. J. *Synth. Met.* **1989**, *32*, 263. (b) MacDiarmid, A. G.; Epstein, A. J. *Synth. Met.* **1994**, *65*, 103. (c) Jiang, H; Geng, Y.; Li, J.; Wang, F. *Synth. Met.* **1997**, *84*, 125.

(12) (a) Kim, B. J.; Oh, S. G.; Han, M. G.; Im, S. S. *Synth. Met.* **2001**, *122*, 297. (b) Han, M. G.; Cho, S. K.; Oh, S. G.; Im, S. S. *Synth. Met.* **2002**, *126*, 53.

(13) Ryu, K. S.; Moon, B. W.; Joo, J.; Chang, S. H. *Polymer* **2001**, *42*, 9355.

(14) Abdiryim, T.; Xiao-Gang, Z.; Jamal, R. *Mater. Chem. Phys.* **2005**, *90*, 367.

(15) Hatchett, D. W.; Josowicz, M.; Janata, J. *J. Phys. Chem. B* **1999**, *103*, 10992.

(16) Huang, L.-M.; Chen, C.-H.; Wen, T.-C.; Gopalan, A. *Electrochim. Acta* **2006**, *51*, 2756.

(17) Paul, R. K.; Pillai, C. K. S. *Polym. Int.* **2001**, *50*, 381.

(18) Pouget, J. P.; Hsu, C. H.; MacDiarmid, A. G.; Epstein, A. J. *Synth. Met.* **1995**, *69*, 119.

(19) Moon, Y. B.; Cao, Y.; Smith, P.; Heeger, A. J. *Polym. Commun.* **1989**, *30*, 196.

(20) Mott, N. F.; Davis, E. A. *Electronic Processes in Non-Crystalline Materials*; Clarendon Press: Oxford, U. K., 1979.

(21) Jung, J. H.; Kim, B. H.; Moon, B. W.; Joo, J.; Chang, S. H.; Ryu, K. S. *Phys. Rev. B* **2001**, *64*, 035101.

(22) Ryu, K. S.; Hong, Y.-S.; Park, Y. J.; Wu, X.; Kim, K. M.; Lee, Y.-G.; Chang, S. H.; Lee, S. J. *Solid State Ionics* **2004**, *175*, 759.

(23) Ryu, K. S.; Kim, K. M.; Kang, S.-G.; Lee, G. J.; Chang, S. H. *Solid State Ionics* **2000**, *135*, 229.

(24) Ryu, K. S.; Kim, K. M.; Kang, S.-G.; Joo, J.; Chang, S. H. *J. Power Sources* **2000**, *88*, 197.

(25) Ryu, K. S.; Kim, K. M.; Park, Y. J.; Park, N.-G.; Kang, M. G.; Chang, S.H. *Solid State Ionics* **2002**, *861*, 152–153.

(26) Ryu, K. S.; Kim, K. M.; Park, N.-G.; Park, Y. J.; Chang, S. H. *J. Power Sources* **2002**, *103*, 305.